Three-dimensional equilibria and island energy transport due to RMP ELM suppression on DIII-D

J.D. King[1], E.J. Strait[1], R. Nazikian[2], C. Paz-Soldan[1], D. Eldon[2], M.E. Fenstermacher[3], N.M. Ferraro[1], J.M. Hanson[4], S.R. Haskey[2], R.J. La Haye[1], M.J. Lanctot[1], S.A. Lazerson[2], N.C. Logan[2], Y.Q. Liu[5], M. Okabayashi[2], J.-K. Park[2], D. Shiraki[6], and A.D. Turnbull[1]

[1]*General Atomics, San Diego, California, USA*

[2]*Princeton Plasma Physics Laboratory, Princeton, New Jersey, USA*

[3]*Lawrence Livermore National Laboratory, Livermore, CA, USA*

[4]*Columbia University, New York, New York, USA*

[5] *Culham Centre for Fusion Energy, Culham Science Centre, Abingdon, Oxfordshire, OX14 3DB, United Kingdom*

[6]*Oak Ridge National Laboratory, Oak Ridge, Tennessee, USA*

email of first author: kingjd@fusion.gat.com

Abstract. Experiments in the DIII-D tokamak show that the plasma responds to resonant magnetic perturbations (RMP) with toroidal mode numbers of $n = 2$ and $n = 3$ without field line reconnection, consistent with resistive magnetohydrodynamic predictions (MHD), while a strong nonlinear bifurcation is apparent when edge localized modes (ELM) are suppressed. The magnetic response associated with this bifurcation is localized to the high field side (HFS) of the machine and exhibits a dominant $n = 1$ component despite the application of a constant amplitude, slowly toroidally rotating, $n = 2$ applied field. The $n = 1$ mode is born locked to the vacuum vessel wall, while the $n = 2$ mode is entrained to the rotating field. Based on these magnetic response measurements, and Thomson scattering measurements of flattening of the electron temperature profile it is likely that these modes are magnetic island chains near the H-mode pedestal. The reduction in ∇T_e occurs near

the $q = 4$ and 5 rational surfaces, suggesting five unique islands are possible ($m = 8$, 9 or 10 for $n = 2$) and ($m = 4$ or 5 for $n = 1$). In all cases, the island width is estimated to be 2 ~ 3 cm. The Chang-Callen calculated confinement degradation due to the presence of an individual island of this size is 8 ~ 12%, which is close to the 13 ~ 14% measured between the ELMing and suppressed states. This suggests that edge tearing modes may alter the pedestal causing peeling-ballooning stability during resonant magnetic perturbation (RMP) induced ELM suppression.

PACS Nos.: 52.55.-s, 52.55.Fa, 52.30.Cv, 52.55.Tn, 52.65.Kj

I. INTRODUCTION

Some years after the discovery of a high confinement regime known as H-mode in the ASDEX tokamak [1] in 1982, there has been a pressing need to understand and ameliorate peeling-ballooning instabilities known as the Type-I edge localized modes [2] (ELM). ELM growth originates near the H-mode pedestal. The mode has a helical filamentary structure that erupts from the low field side (LFS) of tokamak devices [3]. ELMs transport energy and particles radially across the last closed flux surface and into the plasma scrape off layer [4], where field lines intersect the plasma facing components (PFC). For reactor relevant plasmas, ELMs are expected to cause excessive material erosion and unacceptably short lifetimes for PFCs [5] due to their large transient heat and particle loads [6]. These periodic expulsions are not only deleterious to solid surfaces, they also impact core MHD stability [7-10]. Fortunately ELMs can be suppressed through the application of toroidally non-axisymmetric fields known as resonant magnetic perturbations [11] (RMP). The RMP is a static externally applied field that resonates with the plasma at specific edge field helicities, preventing ELM events.

The transport mechanism responsible for modifying the pedestal and causing peeling-ballooning stability is key to understanding RMP ELM suppression. A variety of theories have been proposed to explain this ELM stable pedestal, such as edge field line stochasticity [12], magnetic flutter [13], and magnetic island chain formation [14]. In the case of stochastic transport, overlapping islands are believed to be the cause, and correlations have been found between the width of the q_{95} ELM suppression window (q_{95} is the safety factor at which 95% of the normalized poloidal flux is enclosed, which is typically located near the top of the pedestal) and the degree of predicted stochasticity [15]. However, this model ignores the plasma response to the RMP. It has been shown in DIII-D that the theory of magnetic flutter [13] may be consistent with the electron thermal

diffusivity of nested flux surface regions located between small, non-overlapping magnetic islands near the plasma edge. When compared with inferred edge electron temperature gradient measurements, magnetic flutter diffusivity appears to provide better agreement than that predicted by the presence of small magnetic islands alone [16]. Furthermore, the magnetic flutter model provides an explanation of edge transport in the absence of magnetic islands. This is important, as some evidence has shown that ELM suppression is correlated with an ideal MHD plasma response, which is devoid of islands [17]. A final theory is that non-overlapping magnetic islands of appreciable width are causing significant transport around the H-mode pedestal. Until recently [18,19], this theory has lacked compelling experimental evidence.

Diagnostic complications associated with measurements in the H-mode pedestal have made testing the validity of each of these theories difficult, and has motivated the pursuit of simpler techniques for resolving this critical physics. While major advances in electron cyclotron emission diagnostics have made it possible to resolve two-dimensional images of Alfvén eigenmodes [20] and other MHD [21], measurements in the pedestal are limited due to optical thinness and coarse spatial resolution [22]. Also, the size of many predicted islands is smaller than the radial resolution of most imaging techniques. In an effort to further elucidate these edge dynamics, a millimeter wave imaging reflectometer (MIR) has been installed on DIII-D [23]. While this MIR diagnostic holds great promise, presently an upgraded 3D magnetic diagnostic on DIII-D [24] is providing significant insights into RMP ELM suppression. Most important are sensors located along the high field side (HFS) of the tokamak. For reasons that are continuing to be evaluated, the HFS of the machine exhibits a signature bifurcation in the plasma response at the point of density pumpout [18] and ELM suppression [19], which is not observed along the LFS. These simple magnetic measurements, along with improved resolution in Thomson scattering edge electron temperature measurements

[25], provide strong evidence that the formation of island structures coincide with the onset of RMP ELM suppression.

The mere presence of a magnetic island chain(s) does not confirm any of the previously mentioned theories concerning the cause of RMP ELM suppression. To do this, the island confinement degradation must explain the requisite transport mechanism responsible for maintaining ELM stability during the application of an RMP. This understanding is critical if we are to extrapolate present RMP ELM suppression techniques to burning plasma devices. In this paper we find that largely a laminar kink like structure dominates the HFS plasma response for both $n = 2$ and $n = 3$ RMP's in the absence of ELM suppression. Here we use the word 'laminar' to mean a 3D equilibrium with intact flux surfaces, containing no magnetic islands. Following ELM suppression, the bifurcation in the magnetic response gives rise to the formation of magnetic islands, which individually are estimated to provide a sufficient transport mechanism to cause the observed degradation in energy confinement associated with the application of RMPs.

This paper is organized as follows. The types of DIII-D discharges considered and the method of measuring the perturbed RMP plasma response is described in Sec. II. In Sec. III a comparison of the linear predicted and measured structure of 3D equilibria due to $n = 2$ and $n = 3$ applied magnetic perturbations for a range of values of q_{95} and beta are presented that show largely laminar characteristics. Island width estimations and HFS pedestal bifurcation response measurements are shown in section IV. Section V compares the confinement degradation expected for the measured magnetic island sizes with what is observed based on pressure measurements. Finally, a brief discussion and summary is presented in Sec. VI.

II. EXPERIMENTAL METHOD

The H-mode plasmas studied here had normalized parameters comparable to those expected in the first large volume burning plasma experiments. A diverted lower single null poloidal shape was maintained, with strike point located near the DIII-D lower cryopump. This strong pumping, along with gas injection feedback control, produced constant low density and collisionality. Discharge to discharge, the pedestal electron collisionality, normalized to the trapped thermal bounce frequency, is varied from $\nu^*_{e,ped} \sim 0.18 - 0.5$. These variations in $\nu^*_{e,ped}$ were due to differences in toroidal field, which ranged from B_{T0} = -1.7 T to -2.0 T. As with nearly all DIII-D discharges, the plasma shape is significantly elongated $\kappa \sim 1.8$. The upper and lower triangularity was maintained at $\delta_{upper} \sim 0.3$ and $\delta_{lower} \sim 0.7$, respectively. The plasma response measurements span a range of q_{95} values that include the RMP ELM suppression window. The ELM suppression case presented is achieved through a sufficiently slow variation of the n = 2 field to allow density pumpout to take place, while maintaining the low edge collisionality. For discharges without ELM suppression, the plasma current was varied between 1.1 MA and 1.95 MA, varying the edge safety factor from q_{95} = 3.0 to 4.0.

We study the stable plasma response to externally applied non-axisymmetric (n > 1) fields using detailed magnetic measurements of the 3D tokamak state [24]. These fields were applied using two active sets of 6 “picture-frame” coils located inside the DIII-D tokamak [26] vacuum vessel above and below the outboard midplane of the device (shown in Fig. 1). These coils are referred to as I-coils. An additional external set of 6 coils surrounding the tokamak outboard midplane, known as C-coils, (not shown), were simultaneously energized to correct known n = 1 field errors [27] allowing the plasmas response due to applied n = 2 and n = 3 to be isolated and studied. The poloidal mode content of each toroidal mode is altered by changing the pitch of the applied field between the upper

and lower set of I-coils ($\Delta\phi_{UL}$). The orientation of $\Delta\phi_{UL}$ relative to the current profile is known to significantly impact the 3D state [28]. It is also known to impact the $n = 0$ properties associated with ELM suppression. Two techniques were used for assessing the plasma response.

i. Toroidally rotate the applied field while retaining constant phasing. This is illustrated in Fig. 1 when both of the upper and lower I-coils apply a rotating perturbation at constant frequency and phase difference $\Delta\phi_{UL}$.

ii. Maintain the applied field from a single row of coils static while the other row is rotated in the toroidal direction. This technique both rotates the toroidal phase of the 3D state and continuously varies the $\Delta\phi_{UL}$, and thus the applied field structure.

Both of these applied perturbations allow for synchronous Fourier detection of the external response [29], after which additional spatial decomposition is possible. In all cases the maximum amplitude of I-coil current of 4 kA was used to drive the response. The detailed structural measurements are made along the HFS of the machine since toroidal effects lead to a strong asymmetry between large and small major radius sides of the torus, resulting in a shorter poloidal wavelength and hence more detailed eigenstructure along the HFS.

The structural dependence of 3D equilibria on plasma pressure is beginning to become better understood for $n = 1$ fields [30-33]. However for $n > 1$ perturbations this dependence has largely been relegated to theoretical model predictions [34-36]. To examine possible pressure effects, normalized beta was ramped over a significant range of values [beta is the ratio of plasma pressure to magnetic field pressure and normalized beta is $\beta_N = \beta(aB/I)$, where a is the plasma minor radius, B is the toroidal field and I is the plasma current] using feedback controlled neutral beam injection (NBI).

To determine if the plasma responds to $n > 1$ applied magnetic perturbations in a manner consistent with retaining intact flux surfaces the plasma current was ramped and 3D magnetic response was measured. Three dimensional states, resulting from driving a stable pressure driven kink mode(s) with diverted poloidal shape, have an infinite number of rationale surfaces and should exhibit a continuous variation in the kink mode response as the edge helicity evolves.

III. LAMINAR n = 2 AND n = 3 RESPONSE

Calculations of the magnetic field poloidal harmonic spectrum in the absence of a plasma has shown that higher n non-axisymmetric applied fields are radially localized to the edge [37], and the inclusion of the plasma causes a similar edge localized response [38]. The n = 2 and n = 3 even parity ($\Delta\phi_{UL} = 0^{\circ}$) fields considered in this section have been used for RMP ELM suppression within a q_{95} resonant window [39]. Here we show that in the absence of ELM suppression, the plasma response trends are consistent with a laminar, "smoothly varying," kink response [40].

The n = 3 plasma response amplitude is largely invariant with respect to changes in q_{95} and linearly dependent on β_N. This is shown in Fig. 2, and is qualitatively identical to the n = 2 non-resonant (kink) response trends modeled in Fig. 11 of Ref. 40. In this discharge the plasma current and neutral beam heating were simultaneously increased to survey the 3D response evolution over a trajectory of $\beta_N - q_{95}$ parameter space, which includes the ELM suppression resonant window ($q_{95} \sim$ 11/3). The variation of these key discharge parameters is shown in Fig. 3. Global kink stability limits are known to depend on the plasma internal inductance l_i [41] and in Fig. 2(a) a clear monotonically increasing linear trend in the plasma response amplitude as a function of β_N / l_i is seen. Normalizing the response amplitude by this linear β_N / l_i dependence, it appears that the plasma does not vary significantly with respect to q_{95} [Fig 2(b)]. The plasma response amplitude only shows a weak decreasing trend along the HFS, and along the LFS the response is invariant with respect to

q_{95}. This independence of the plasma response with respect to q_{95} is opposite to modeling of resonant field amplification due to "edge" peeling modes [42], providing further evidence that the structure of these 3D equilibria is due to a "global" kink mode.

However, this lack of response variation in q_{95} is somewhat counter-intuitive, partly because applied $n = 3$ fields are known to resonate with q_{95} during ELM suppression (pumpout) giving rise to macroscopic changes in axisymmetric edge pressure and current profiles. This discharge has identical plasma conditions, and applied RMP amplitude, as previous ELM suppressed cases, with the exception slightly higher edge collisionality. Since these observations (Fig. 2) are consistent with a kink mode response, and no appreciable impact to the ELM activity is observed, it may be reasonable to surmise that a purely laminar kink distortion (no reconnected flux surfaces) does not fully describe RMP ELM suppression dynamics.

For this laminar kink, we find the response along the HFS exhibits a smooth dependence on the edge helicity of the plasma, which is mostly captured using a resistive MHD code. Toroidal effects lead to a strong asymmetry between LFS and HFS of the torus, and previous modeling of displacements [43,44] has found that the eigenmodes generally have shorter poloidal wavelength along the HFS. Considering detailed measurements of 3D equilibria using the full poloidal spatial resolution of the HFS 3D magnetics it is seen in Fig. 4 that the plasma response is strongly dependent on q_{95} for both $n = 2$ and $n = 3$ applied perturbations, unlike the midplane measurements of Fig. 2. In Fig. 4 the measured q_{95} evolution of the response at a single toroidal phase is compared with single-fluid MHD model predictions including Spitzer resistivity using the MARS-F code [45,38]. While resistivity is included, calculations with resistivity set to zero showed no appreciable difference in the modeled response for these cases, suggesting ideal MHD can capture the observed trends. To approximate the evolution of the q-profile during experimental I_P ramps, the equilibrium

inputs for each case are generated by the Grad-Shafranov solver of the CORSICA code [46] with the total plasma current scaled from a single starting axisymmetric kinetic EFIT [47] equilibrium reconstruction. To avoid core instability in these calculations the minimum q on-axis is maintained greater than 1.05 during these equilibria rescalings. Both model and measurement show that the detailed structure moves up the wall as q_{95} increases. These variations are consistent with increasing edge helicity. Resistive MHD largely captures the mode structure within this (β_N, q_{95}) parameter space. There is quantitative agreement in amplitude throughout the n = 3 case. However, quantized shifts are predicted as the truncated edge safety factor (q_a) approaches rational surfaces (m/3 and m/2). This is likely a truncation artifact and is not observed in experiment. The actual experimental axisymmetric equilibrium is diverted, and has an infinite number of rational surfaces. This is because q_a approaches infinity at the seperatrix. While caution is needed in equilibrium truncation near rational surfaces, resistive MHD is accurately describing the measured plasma response to edge localized higher n perturbations. This agreement, along with other recent studies [30,31,48], provides mounting evidence that laminarly displaced nested flux surfaces are sufficient to describe the general plasma response to applied magnetic perturbations for a large portion of tokamak operating space.

The data and modeling span the q_{95} resonance for n = 3 RMP ELM suppression (q_{95} ~ 11/3), although no ELM suppression is achieved in this discharge. In this case ELM suppression is avoided by maintaining edge collisionality slightly higher than is typically required. Interestingly, no strong resonance in the magnetic response is predicted or measured. This stands in stark contrast to recent observations during n = 2 RMP experiments on DIII-D, which show a distinct modification of the plasma response along the HFS at the onset of suppression [18,19]. The details of this finding will be discussed in section VI.

Modeling a larger range of q_{95} plasma response along the HFS of the machine demonstrates changes in eigenmode wavelength that are characteristic of a laminar kink mode response. Specifically the poloidal wavelength decreases as q_{95} increases, which is consistent with decreased edge field pitch. In Fig. 5 the average poloidal wavelength of the eigenstructure is shown. The average is taken over the entire height of the inner wall. The decrease in the predicted poloidal wavelength is essentially continuous, which is expected for a purely laminar response. This shows that the helicity of the dominant kink mode is decreasing as q_{95} increases for both $n = 2$ and $n = 3$. Note that the q_{95} invariance of the response amplitude along the LFS (Fig. 2) is largely a consequence of a large poloidal wavelength at the outer midplane.

The $n = 2$ perturbation gives rise to a kink with ~1.65 times larger poloidal wavelength than the $n = 3$. In a circular large aspect ratio tokamak kink modes have external structure consisting of only a single dominant poloidal and toroidal harmonic, m and n, respectively [49]. The structure for this simple kink is defined by the finite $q_{a,}$ where $m/n \sim q_a$. In diverted plasmas q_a is infinite and q_{95} serves as a proxy to the wall-limited q_a in describing the edge helicity of the field pitch. A wavelength ratio of 3/2 is expected between the $n = 2$ and $n = 3$ kink modes, assuming a circular cross-section cylindrical approximation with constant edge helicity and a single poloidal harmonic. This ratio is consistent with the model result (Fig. 5) that includes toroidal and poloidal shaping effects.

Taken together these figures show that for $n > 1$, the plasma is responding as expected for a stable pressure driven kink mode. A kink structure smoothly varies with the pitch of the field. Although resonant screening currents, localized at rational surfaces, can impact the amplitude of the measured response at the wall, the pitch of the kink should exhibit a continuous change.

In this section we have mapped the plasma response dependence of H-mode discharges on q_{95} for fixed external applied field (even parity phasing), in much the same way as has recently been modeled using MARS-F code [40], except now we are able to compare with detailed measurements [10]. In the following section we examine the nonlinear phasing dependence of the plasma response during $n = 2$ RMP ELM suppression with fixed q_{95}.

IV. ISLAND FORMATION DURING ONSET OF n = 2 ELM SUPPRESSION

The observations in the previous section stand in stark contrast to the nonlinear bifurcation observed during $n = 2$ RMP ELM suppression. Rather than smooth trends as q_{95} is changed, a rapid transition is seen in the response amplitude, and toroidal mode content, as a small change in the poloidal spectrum (phasing) is applied. This bifurcation in the magnetic response near the HFS midplane is shown in Fig. 6(a). In this figure we present a toroidal fit to 8 magnetic sensor pair measurements of the vertical component of the non-axisymmetric plasma response. The time spans an ELM suppression period, which is only observed for $0^{\circ} \leq \Delta\phi_{UL} \leq 45^{\circ}$. The contour shows the combined plasma response due to both $n = 1$ and $n = 2$ components of the field. The $n = 1$ component of the field dominates the response, despite the application of an $n = 2$ RMP. The fact that ELM suppression correlates with the presence of this additional $n = 1$ response provides a potential connection to previous observations during the application of $n = 3$ RMP fields. Those previous $n = 3$ experiments showed that the addition of an $n = 1$ field expands the resonant q_{95} window over which ELMs are suppressed [6].

For fixed q_{95}, altering the phasing between the upper and lower set of I-coils varies the poloidal mode content of the applied field, providing an alternative path for understanding the resonant nature of RMP ELM suppression. In this experiment, the lower I-coils are energized with phase fixed to the lab frame, while the upper coil phase is rotated toroidally at 1 Hz. This variation in the

phasing means that the applied field orientation at the q = 4, 4.5 and 5.0 flux surfaces range from being orthogonal to aligned with the pitch of this surface [40]. When the perturbation is roughly aligned with the pitch of the rational surface it is producing the strongest drive toward opening up a magnetic island. However recent ideal and resistive MHD modeling of these cases has shown that pumpout [18] and corresponding ELM suppression [19], do not correspond exactly to the peak in edge resonant field $\Delta\phi_{UL} \approx 0^{\circ}$. Furthermore, careful examination of spontaneous transitions out of ELM suppression previously showed the unlocking of an n = 1 tearing-like structure [19]. In the event that this magnetic bifurcation in the response is due to n = 1 and n = 2 locked tearing modes, it is then possible to estimate their island sizes. Also, based on the island width and poloidal mode number it is possible to determine if the resulting confinement degradation is sufficient to return the edge to peeling-ballooning stability.

The observation of n = 1 and n = 2 modes during ELM suppression (Fig. 6), with amplitude beyond that expected and measured for pure kink response, suggest that magnetic islands have formed. After the onset of ELM suppression (t ~ 4705 *ms*) a non-rotating n = 1 mode grows to ~ 3.5 G (not shown). At the same time an n = 2 mode of ~1.8 G (not shown) is observed to be entrained with the rotating field of the I-coils. Both the locked nature of the n = 1 and entrained nature of the n = 2 are evidenced by the phase traces of Fig. 6(c), where the n = 1 shows essentially no variation in phase over the ELM suppression window, consistent with locking to the vacuum vessel wall, while the n = 2 phase changes by ~ 40°, which is consistent with the 45° variation applied during this time interval. The modeling and measurement of the kink mode response along the HFS in Fig. 4(b,d) is about 33% less than is observed n = 2 mode amplitude. It should also be noted that the amplitude of the response increases rapidly despite a subtle change in the applied

phasing. This transition is inconsistent with a simple kink mode picture, where variations in the response trend like $|\cos(\Delta\phi_{UL}/2)|$ [18,48].

The island size can be estimated using an approximation assuming ellipsoidal elongated plasma cross-section and large aspect ratio. Since the DIII-D tokamak has a modest aspect ratio of 2.7, it is necessary to apply an empirical correction factor, which is determined from direct internal island width measurement using ECE radiometry [50]. Using this correction, the island width can be determined from dB/dt measured mode amplitudes along the HFS. Here we are measuring the integrated amplitude $\tilde{B}_\theta$ of the vertical component of the mode. Since the toroidal rotation of the modes is between 0 and 1 Hz, we can neglect resistive wall eddy currents and convert this wall measured poloidal field $\tilde{B}_\theta$ into a radial field amplitude at each rational surfaces minor radius r using,

$$\left|\tilde{B}_r\right| = \left(\frac{b}{r}\right)^{m+1} \left|\tilde{B}_\theta\right|_{wall}, \qquad (1)$$

where the inboard probe minor radius is b. The island width is then approximated to be,

$$w \approx 0.68 \left(\frac{16 r R_0 |\tilde{B}_r|}{m s B_{\phi 0}}\right)^{1/2}, \qquad (2)$$

where $s = r(dq/dr)/q^2$, R_0 is the major radius of the rational surface, and the factor of 0.68 is the empirical correction determined from previous experiments [51]. The radii of the 4/1,9/2 and 5/1 rational surfaces are determined from equilibrium calculations using the EFIT code [47]. The poloidal mode numbers m = 8, 9, and 10, for n = 2, and m = 4 and 5, for n = 1, are considered since Thomson electron pressure measurements exhibit a strong change in gradient near $4.0 < q < 5.0$ rational surfaces. It should be emphasized that we do not propose two island chains exist simultaneously on the same rational surface. Instead, we are simply examining the energy transport

associated with either possible island being present at each surface.

Instead of the two separate decoupled modes, it is possible that a single island chain contains both $n = 1$ and $n = 2$ components. If the islands within either a single 8/2, or 10/2 chain are asymmetric, then a 4/1 or 5/1 additional component may be detected, respectively. While plausible, we only wish to note this possibility here without further discussion. Future analysis, as well as additional internal diagnostic coverage, should enable this idea to be tested.

In the case of two separate islands, we deduce that the $n = 1$ island exists on either the $q = 4$ or 5 surface and hypothesize that the $n = 2$ rational surfaces are near the pedestal. A benign 2/1 neoclassical tearing mode (NTM) that is rapidly rotating at ~19 kHz, occupies the $q = 2$ rational surface, eliminating it as a candidate. Also, the minimum safety factor is maintained greater than 1 throughout the discharge, such that a 1/1 could not be stimulated. For the $n = 1$ mode this leaves the 5/1, 4/1 and 3/1 rational surfaces as possible island chain locations. Since no strong rotation shear is observed near the $q = 3$ surface, which would be expected if a wall locked island were present there, it appears that the $q = 4$ or 5 surfaces are the most plausible radial locations for the observed $n = 1$ mode. These surfaces correspond to the top and foot of the pedestal. Assuming the $n = 2$ island is originating near this same location there exist 3 rational surfaces possible $q = 8/2$, 9/2, and 10/2. It should also be noted that it is possible two $n = 1$ islands (or two $n = 2$ islands) are locked together.

Unfortunately, distinguishing the detailed poloidal structure of both stationary modes is not currently possible on DIII-D using the upgraded magnetic diagnostic. The high spatial resolution 3D sensor array along the HFS wall measures a single component of the field at only two toroidal locations, which prohibits multiple toroidal modes from being resolved simultaneously [24]. Note, resolving the m for multiple rotating modes requires one spatial dimension fewer sensors, and is well within the previous diagnostic capabilities of the DIII-D magnetic system [52]. Future work will

focus on further elucidating the poloidal structure of these modes.

Despite appreciably larger mode amplitude (G), the 4/1 or 5/1 island width (cm) is comparable to the potential 8/2, 9/2 or 10/2 islands. Figure 6(b) shows that the peak island widths are approximately 2.8 to 2.2 cm for the $n = 1$ and $n = 2$ modes, respectively. For islands of the same n, the high m's and nearly identical (b/r) values of Eqn. (1) and (2) lead to only a small (~ 5 %) difference in the estimated widths. These estimated widths are consistent with Thomson scattering T_e measurements along the LFS plasma edge (Fig. 7). During ELM suppression [Fig. 7(a), 4700 – 4850 ms] the overall temperature near the edge decreases by ~15% in the vicinity of the $q = 4/1$, 9/2 and 5/1 rational surfaces. Also, the gradient on either side of the 9/2 surface is flattened [Fig. 7(b)]. Within the experimental uncertainty of the measurement, this flat region, which is correlated to ELM suppression [Fig. 7(b) – blue], extends ~1.7 cm beyond that observed in the absence of ELM suppression [Fig. 7(b) – red]. The flattening of the temperature profile near a rational surface is consistent with very large energy transport across magnetic islands.

To be clear, the Thomson scattering measurements shown in Fig. 7 exhibit only temperature changes that are consistent with the presence of magnetic islands. A definitive experimental signature of the presence of these magnetic islands is still necessary. Specifically, the internal observation of phase inversions about the rational surfaces is needed. It is planned in future work to entrain the islands with both applied $n = 2$ and $n = 1$ fields, and rotate the islands past the chords of the toroidally fixed profile diagnostics. This would enable the characteristic oscillations, as the X and O points traverse the chords, to be observed.

V. ISLAND CONFINEMENT DEGRADATION

RMP ELM suppression reduces the H-mode pedestal height causing some degradation to global energy confinement. This confinement degradation is quantifiable as the difference in plasma stored

energy. Also, an estimate of the confinement degradation associated with an island is possible assuming that the island results in short circuited energy confinement, which causes a local flattening of the axisymmetric pressure profile at the mode rational surface. We find that the estimated confinement degradation associated with either the $n = 1$ or $n = 2$ pedestal island is sufficient to explain the drop in stored energy that occurs during ELM suppression.

We turn to a simple energy confinement degradation estimation of the Chang – Callen island model [53] that assumes constant density n, energy diffusivity χ, and heat sources throughout the plasma volume, except at the location of the magnetic island where infinite χ is assumed giving rise to a flat spot in the temperature profiles. The assumption of constant χ provides an upper bound to the estimated degradation. Realistic χ profiles increase toward the plasma edge such that the additional loss in confinement due to an island has a smaller overall impact. However, by considering only the rational surface inside of the pedestal ($q = 4$), where the radial gradient of χ is much less steep, the degradation estimate should be reasonable. Based on a 2 ~ 3 cm wide island we would expect a corresponding global confinement decrease of 8 ~ 12 %. This is consistent with the experimentally observed confinement degradation of 13 ~ 14 % during ELM suppression. This experimental confinement degradation can be seen in Fig. 8, for EFIT equilibrium reconstructions before (4700 ms) and after (4780 ms) ELM suppression. The dotted line corresponds to the degraded pressure once RMP ELM suppression has taken place while the pressure profile just before suppression is shown as a solid line. Note that the injected power is constant for both of these cases, such that the only thing changing is the transport associated with the applied RMP.

The transport associated with the presence of individual islands is sufficient to account for the entire change in energy confinement. That said the bifurcation in both $n = 1$ and $n = 2$ magnetic responses, suggests that more than one island may be present at the same time. We speculate that the

$n = 2$ island may be located at nearby rationale surfaces inside or outside $q = 4$. In either case it is clear that the estimated island transport alone can provide the dominant contribution to the observed edge transport.

VI. DISCUSSION AND CONCLUSIONS

In conclusion, we have shown that in the absence of ELM suppression the plasma responds in a purely linear laminar manner to the application of RMPs. This is true for both $n = 2$ and $n = 3$ perturbations. The response bifurcates nonlinearly at the onset of $n = 2$ RMP ELM suppression, providing a signature magnetic plasma response along the HFS of DIII-D with dominant $n = 1$ and smaller $n = 2$ that suggests multiple magnetic islands emerge. The island chains are estimated to be approximately 2 ~ 3 cm wide and are born locked. The $n = 1$ is locked to the wall, where as the $n = 2$ appears to be entrained by the rotating RMP. Individually the presence of these magnetic islands may be sufficient to explain the resulting increased edge energy transport responsible for maintaining ELM stability.

The individual island transport associated with the Chang – Callen island model [53] closely predicts the observed pedestal confinement degradation. The bifurcation to a state with islands at the time of ELM suppression, and the agreement with the Chang-Callen model, are evidence that island transport plays a key role. It is conceivable that any deficit in the predicted energy confinement degradation could be due to magnetic flutter, which is not accounted for in this simple approximation. However, it is also possible that non-overlapping $n = 1$ and $n = 2$ islands co-exist on different rational surfaces at the top and foot of the H-mode pedestal, in which case additional transport may be accounted for without requiring magnetic flutter theory. The present static non-axisymmetric magnetic measurement capabilities of DIII-D are insufficient to resolve the poloidal mode number associated with each toroidal mode and future work will be dedicated to further

elucidating these mode structures.

The evidence concerning these island estimations represent a coarse effort to determine the transport mechanisms associated with RMP ELM suppression and much additional work is required to confirm these suspicions. While these estimates prove useful in approximating the transport [53] associated with a variety of macroscopic MHD, the details of how the RMP allows a magnetic island to open must be understood on a first principles level. This is the subject of future work in which detailed nonlinear 3D resistive models like the M3D-C1 code [54] are used to resolve the onset of this critical transport mechanism in detail and validate its onset. This detailed determination of island opening and transport is also needed to effectively extrapolate to next step burning plasma tokamak devices.

In addition to this transport mechanism, it is important that the underlying dynamics leading to the ELM stable state be understood, and that these $n = 2$ dynamics be the same for all higher n ELM suppression. The interplay between the $n = 2$ and $n = 1$ response is still unknown. We hypothesize that the edge localized $n = 2$ kink response initiates edge density pumpout, however the mechanism for this transient is not known. We speculate that the reduced edge collisionality, caused by pumpout, enables field penetration of a residual $n = 1$ error field that leads to island locking. This locked island provides the transport mechanism for maintaining stable pedestal current and pressure profiles.

A further question that requires additional analysis is, why these magnetic islands are not observed on the LFS of the machine? At this point we speculate that the LFS response due to the island is masked by the kink mode response due to ballooning unfavorable curvature. Such response should be predominantly $n = 2$ and not exhibit a large $n = 1$ amplitude. If true, this provides a possible reason why DIII-D, with its 3D magnetic diagnostic along the HFS, is the first to observe

this island effect.

ACKNOWLEDGEMENTS

This material is based upon work supported by the U.S. Department of Energy, Office of Science, Office of Fusion Energy Sciences, using the DIII-D National Fusion Facility, a DOE Office of Science user facility, under Awards DE-FC02-04ER54698, DE-AC02-09CH11466, DE-AC52-07NA27344, DE-FG02-04ER54761 and DE-AC05-00OR22725. DIII-D data shown in this paper can be obtained in digital format by following the links at https://fusion.gat.com/global/D3D_DMP. The authors wish to thank R. Buttery for suggesting the possibility that both mode responses could be due to a single island structure. We also wish to acknowledge A. Rieman for many fruitful model validation discussions.

REFERENCES

[1] F. Wagner, G. Becker, K. Behringer, D. Campbell, A. Eberhagen, W. Engelhardt, G. Fussmann, O. Gehre, J. Gernhardt, G.V. Gierke, G. Haas, M. Huang, F. Karger, M. Keilhacker, O. Klüber, M. Kornherr, K. Lackner, G. Lisitano, G.G. Lister, H.M. Mayer, D. Meisel, E.R. Müller, H. Murmann, H. Niedermeyer, W. Poschenrieder, H. Rapp, H. Röhr, F. Schneider, G. Siller, E. Speth, A. Stäbler, K.H. Steuer, G. Venus, O. Vollmer, and Z. Yü, *Phys. Rev. Lett.* **49**, 1408, (1982).

[2] P.B. Snyder, H.R. Wilson, J.R. Ferron, L.L. Lao, A.W. Leonard, T.H. Osborne, A.D. Turnbull, D. Mossessian, M. Murakami, X.Q. Xu, *Phys. Plasmas* **9**, 2037 (2002).

[3] A. Kirk, H.R. Wilson, G.F. Counsell, R. Akers, E. Arends, S.C. Cowley, J. Dowling, B. Lloyd, M. Price, M. Walsh, and MAST Team, *Phys. Rev. Lett.* **92**, 245002 (2004).

[4] J.A. Boedo, D.L. Rudakov, E. Hollmann, D.S. Gray, K.H. Burrell, R.A. Moyer, G.R. McKee, R. Fonck, P.C. Stangeby, T.E. Evans, P.B. Snyder, A.W. Leonard, M.A. Mahdavi, M.J. Schaffer, W.P. West, M.E. Fenstermacher, M. Groth, S.L. Allen, C. Lasnier, G.D. Porter, N.S. Wolf, R.J. Colchin, L. Zeng, G. Wang, J.G. Watkins, T. Takahashi, and DIII-D Team, *Phys. Plasmas* **12**, 072516 (2005).

[5] A. Loarte, G. Huijsmans, S. Futatani, L.R. Baylor, T.E. Evans, D.M. Orlov, O. Schmitz, M. Becoulet, P. Cahyna, Y. Gribov, A. Kavin, A. Sashala Naik, D.J. Campbell, T. Casper, E. Daly, H.

Frerichs, A. Kischner, R. Laengner, S. Lisgo, R.A. Pitts, G. Saibene, and A. Wingen, *Nucl. Fusion* **54**, 033007 (2014).
[6] M.E. Fenstermacher, A.W. Leonard, P.B. Snyder, J.A. Boedo, N.H. Brooks, R.J. Colchin, D.S. Gray, R.J. Groebner, M. Groth, E.M. Hollmann, C.J. Lasnier, T.H. Osborne, T.W. Petrie, D.L. Rudakov, H. Takahashi, J.G. Watkins, L. Zeng, and the DIII-D Team, *Plasma Phys. Control. Fusion* **45**, 1597 (2003).
[7] Z. Chang and J.D. Callen, *Phys. Rev. Lett.* **74**, 4663 (1995).
[8] D.P. Brennan, S.E. Kruger, T.A. Gianakon, and D.D. Schnack, *Nucl. Fusion* **45**, 1178 (2005).
[9] S.P. Gerhardt, D.P. Brennan, R. Buttery, R.J. La Haye, S. Sabbagh, E. Strait, M. Bell, R. Bell, E. Fredrickson, D. Gates, B. LeBlanc, J. Menard, D. Stutman, K. Tritz, and H. Yuh, *Nucl. Fusion* **49**, 032003 (2009).
[10] J.D. King, R.J. La Haye, C.C. Petty, T.H. Osborne, C.J. Lasnier, R.J. Groebner, F.A. Volpe, M.J. Lanctot, M.A. Makowski, C.T. Holcomb, W.M. Solomon, S.L. Allen, T.C. Luce, M.E. Austin, W.H. Meyer, and E.C. Morse, *Phys. Plasmas* **19**, 022503 (2012).
[11] T. E. Evans, R. A. Moyer, P. R. Thomas, J. G. Watkins, T. H. Osborne, J. A. Boedo, E. J. Doyle, M. E. Fenstermacher, K. H. Finken, R. J. Groebner, M. Groth, J. H. Harris, R. J. La Haye, C. J. Lasnier, S. Masuzaki, N. Ohyabu, D. G. Pretty, T. L. Rhodes, H. Reimerdes, D. L. Rudakov, M. J. Schaffer, G. Wang, and L. Zeng, *Phys. Rev. Lett.* **92,** 235004 (2004).
[12] O. Schmitz, T.E. Evans, M.E. Fenstermacher, E.A. Unterberg, M.E. Austin, B.D. Bray, N.H. Brooks, H. Frerichs, M. Groth, M.W. Jakubowski, C.J. Lasnier, M. Lehnen, A.W. Leonard, S. Mordijck, R.A. Moyer, T.H. Osborne, D. Reiter, U. Samm, M.J. Schaffer, B. Unterberg, and W.P. West, *Phys. Rev. Lett.* **103**, 165005 (2009).
[13] J.D. Callen, C.C. Hegna, A.J. Cole, *Nucl. Fusion* **53**, 113015 (2013).
[14] M.R. Wade, R. Nazikian, J.S. deGrassie, T.E. Evans, N.M. Ferraro, R.A. Moyer, D.M. Orlov, R.J. Buttery, M.E. Fenstermacher, A.M. Garofalo, M.J. Lanctot, G.R. McKee, T.H. Osborne, M.A. Shafer, W.M. Solomon, P.B. Snyder, W. Suttrop, A. Wingen, E.A. Unterberg, and L. Zeng, *Nucl. Fusion* **55**, 023002 (2015).
[15] M.E. Fenstermacher, T.E. Evans, T.H. Osborne, M.J. Schaffer, M.P. Aldan, J.S. deGrassie, P. Gohil, I. Joseph, R.A. Moyer, P.B. Snyder, R.J. Groebner, M. Jakubowski, A.W. Leonard, O. Schmitz, and the DIII-D team, *Phys. Plasmas* **15**, 056122 (2008).

[16] S.P. Smith, Bull. Am. Phys. Soc. Div. *Plasma Phys.* Abstract ID: BAPS.2013.DPP.NI2.5, (2013).
[17] M.J. Lanctot, R.J. Buttery, J.S. de Grassie, T.E. Evans, N.M. Ferraro, J.M. Hanson, S.R. Haskey, R.A. Moyer, R. Nazikian, T.H. Osborne, D.M. Orlov, P.B. Snyder, M.R. Wade, and the DIII-D Team, *Nucl. Fusion* **53**, 083019 (2013).
[18] C. Paz-Soldan, R. Nazikian, S.R. Haskey, N.C. Logan, E.J. Strait, N.M. Ferraro, J.M. Hanson, J.D. King, M.J. Lanctot, R.A. Moyer, M. Okabayashi, J.-K. Park, M.W. Shafer, and B.J. Tobias, *Phys. Rev. Lett.* **114**, 105001 (2015).
[19] R. Nazikian, C. Paz-Soldan, J.D. Callen, J.S. deGrassie, D. Eldon, T.E. Evans, N.M. Ferraro, B.A. Grierson, R.J. Groebner, S.R. Haskey, C.C. Hegna, J.D. King, N.C. Logan, G.R. McKee, R.A. Moyer, M. Okabayashi, D.M. Orlov, T.H. Osborne, J-K. Park, T.L. Rhodes, M.W. Shafer, P.B. Snyder, W.M. Solomon, E.J. Strait, and M.R. Wade, *Phys. Rev. Lett.* **114**, 105002 (2015).
[20] B.J. Tobias, I.G.J. Classen, C.W. Domier, W.W. Heidbrink, N.C. Luhmann, Jr., R. Nazikian, H.K. Park, D.A. Spong, and M.A. Van Zeeland, *Phys. Rev. Lett.* **106**, 075003 (2011).
[21] B. Tobias, L. Yu, C.W. Domier, N.C. Luhmann, Jr., M.E. Austin, C. Paz-Soldan, A.D. Turnbull, I.G.J. Classen, and the DIII-D Team, *Plasma Phys. Control. Fusion* **55**, 095006 (2013).
[22] B.J. Tobias, M.E. Austin, J.E. Boom, K.H. Burrell, I.G.J. Classen, C.W. Domier, N.C. Luhmann, Jr., R. Nazikian, and P.B. Snyder, *Rev. Sci. Instrum.* **83**, 10E329 (2012).
[23] C.M. Muscatello, C.W. Domier, X. Hu, G.J. Kramer, N.C. Luhmann, Jr., X. Ren, P. Riemenschneider, A. Spear, B.J. Tobias, E. Valeo, and L. Yu, *Rev. Sci. Instrum.* **85**, 11D702 (2014).
[24] J.D. King, E.J. Strait, R.L. Boivin, D. Taussig, M.G. Watkins, J.M. Hanson, N.C. Logan, C. Paz-Soldan, D.C. Pace, D. Shiraki, M.J. Lanctot, R.J. La Haye, L.L. Lao, D.J. Battaglia, A.C. Sontag, S.R. Haskey, and J.G. Bak, *Rev. Sci. Instrum.* **85**, 083503 (2014).
[25] D. Eldon, B.D. Bray, T.M. Deterly, C. Liu, M. Watkins, R.J. Groebner, A.W. Leonard, T.H. Osborne, P.B. Snyder, R.L. Boivin, and G.R. Tynan, *Rev. Sci. Instrum.* **83**, 10E343 (2012).
[26] J.L. Luxon, *Nucl. Fusion* **42**, 614 (2002).
[27] J.L. Luxon, M.J. Schaffer, G.L. Jackson, J.A. Leuer, A. Nagy, J.T. Scoville, and E.J. Strait, *Nucl. Fusion* **43**, 1813 (2003).
[28] M.J. Lanctot, H. Reimerdes, A. M. Garofalo, M. S. Chu, Y.Q. Liu, E.J. Strait, G.L. Jackson, R.J. La Haye, M. Okabayashi, T.H. Osborne, and M.J. Schaffer, *Phys. Plasmas* **17**, 030701 (2010).

[29] H. Reimerdes, M.S. Chu, A.M. Garofalo, G.L. Jackson, R.J. La Haye, G.A. Navratil, M. Okabayashi, J.T. Scoville, and E.J. Strait, *Phys. Rev. Lett.* **93**, 135002 (2004).
[30] J.D. King, E.J. Strait, S.A. Lazerson, N.M. Ferraro, N.C. Logan, S.R. Haskey, J.-K. Park, J.M. Hanson, M.J. Lanctot, Y.Q. Liu, R. Nazikian, M. Okabayashi, C. Paz-Soldan, D. Shiraki, and A.D. Turnbull, *Phys. Plasmas* **22**, 072501 (2015).
[31] M.J. Lanctot, H. Reimerdes, A.M. Garofalo, M.S. Chu, J.M. Hanson, Y.Q. Liu, G.A. Navratil, I.N. Bogatu, Y. In, G.L. Jackson, R.J. La Haye, M. Okayabashi, J.-K. Park, M.J. Schaffer, O. Schmitz, E.J. Strait, and A.D. Turnbull, *Phys. Plasmas* **18,** 056121 (2011).
[32] Z.R. Wang, M.J. Lanctot, Y.Q. Liu, J-K. Park, and J.E. Menard, *Phys. Rev. Lett.* **114**, 145005 (2015).
[33] J.D. King, E.J. Strait, N.M. Ferraro, J.M. Hanson, S.R. Haskey, M.J. Lanctot, Y.Q. Liu, N.Logan, C. Paz-Soldan, D. Shiraki, and A.D. Turnbull, *Phys, Rev. Lett.* (submitted).
[34] J.-K. Park, A.H. Boozer, and A.H. Glasser, *Phys. Plasmas* **14,** 052110 (2007).
[35] Y.Q. Liu, A. Kirk, Y. Gribov, M.P. Gryaznevich, T.C. Hender, and E. Nardon, *Nucl. Fusion* **51**, 083002 (2011).
[36] Y.Q. Liu, A. Kirk, Y. Sun, P. Cahyna, I.T. Chapman, P. Denner, G. Fishpool, A.M. Garofalo, J.R. Harrison, E. Nardon, *Plasma Phys. Control. Fusion* **54**, 124013 (2012).
[37] M.J. Schaffer, J.E. Menard, M.P. Aldan, J.M. Bialek, T.E. Evans, and R.A. Moyer, *Nucl. Fusion* **48**, 024004 (2008).
[38] Y.Q. Liu, A. Kirk, and E. Nardon, *Phys. Plasmas* **17,** 122502 (2010).
[39] T.E. Evans, R.A. Moyer, K.H. Burrell, M.A. Fenstermacher, Ilon Joseph, A.W. Leonard, T.H. Osborne, G.D. Porter, M.J. Schaffer, P.B. Snyder, P.R. Thomas, J.G. Watkins, and W.P. West, *Nature Physics* **2**, 419-423 (2006).
[40] S.R. Haskey, M.J. Lanctot, Y.Q. Liu, J.M. Hanson, B.D. Blackwell, and R. Nazikian, *Plasma Phys. Control. Fusion* **56**, 035005 (2014).
[41] E.J. Strait, *Fusion Sci. Technol.* 48, 864 (2005).
[42] Y.Q. Liu, S. Saarelma, M.P. Gryaznevich, T.C. Hender, D.F. Howell and JET-EFDA contributors, *Plasma Phys. Control. Fusion* **52**, 045011 (2010).
[43] A.D. Turnbull, *Nucl. Fusion* **52**, 054016 (2012).

[44] A.D. Turnbull, N.M. Ferraro, V.A. Izzo, E.A. Lazerus, J.K. Park, W.A. Cooper, S.P. Hirshman, L.L. Lao, M.J. Lanctot, S. Lazerson, Y.Q. Liu, A. Reiman, and F. Turco, *Phys. Plasmas* **20**, 056114 (2013).

[45] Y.Q. Liu, A. Bondeson, C. M. Fransson, B. Lennartson, and C. Breitholtz, *Phys. Plasmas* **7,** 3681 (2000).

[46] J. Crotinger, "Corsica: A comprehensive simulation of toroidal magnetic fusion devices," Lawrence Livermore National Laboratory Technical Report UCRL-ID- 126284 (1997).

[47] L.L. Lao, H. St. John, R.D. Stambaugh, A.G. Kellman and W. Pfeiffer, *Nucl. Fusion* **25**, 1611 (1985).

[48] S.R. Haskey, M.J. Lanctot, Y.Q. Liu, C. Paz-Soldan, J.D. King, B.D. Blackwell, and O. Schmitz, *Plasma Phys. Control. Fusion* **57**, 025015 (2015).

[49] J. Wesson, "Tokamaks: 2nd Edition," Clarendon Press – Oxford (1997).

[50] R.J. La Haye, R.J. Buttery, S. Guenter, G.T.A. Huysmans, M. Maraschek, H.R. Wilson, *Phys. Plasmas* **7**, 3349 (2000).

[51] Z. Chang, E.D. Fredrickson, S.H. Batha, M.G. Bell, R.V. Budny, F.M. Levinton, K.M. McGuire, G. Taylor, M.C. Zarnstorff, and TFTR Group, *Phys. Plasmas* **5**, 1076 (1998).

[52] E.J. Strait, *Rev. Sci. Instrum.* **77**, 023502 (2006).

[53] Z. Chang and J.D. Callen, *Nucl. Fusion* **30**, 219 (1990).

[54] N.M. Ferraro, *Phys. Plasmas* **19**, 056105 (2012).

FIGURE CAPTIONS

Figure 1 (color online): Illustration of a full 3D n=2 normal field displacement δB_n for a three-dimensional tokamak equilibria perturbation (contours), DIII-D I-coils (green), HFS magnetic sensor locations (blue), and an example 60° phase difference between the upper and lower coil sets $\Delta\phi_{UL}$ (white + indicates identical coil currents). For rotating the entire perturbation the coils with the + symbol apply identical sinusoidal oscillating waveforms. For rotating $\Delta\phi_{UL}$, only the upper or lower row of coil currents are oscillated.

Figure 2 (color online): The measured LFS and HFS midplane δB_p plasma response amplitude for $n = 3$ even parity applied field (a) normalized to the applied perturbing current for a range of β_N/l_i. (b) normalized to β_N/l_i and the applied current, showing no variation in q_{95} when pressure and stability effects are factored out. Discharge 153585.

Figure 3 (color online): For discharge 153585 (a) the red trace is plasma current (MA), blue β_N, (b) the total neutral beam injected power (MW), (c) the safety factor at the flux surface enclosing 95% of the poloidal flux, (d) the D-alpha emissions correlated with wall recycling caused by ELMs (e) the measured response of a single LFS midplane magnetic sensor pair (G), and (f) the plasma internal inductance evolution.

Figure 4 (color online): HFS poloidal field measured magnetic response eigenstructure at a fixed toroidal phase for (a) $n = 3$ applied perturbations for discharge 153585, (b) $n = 2$ applied perturbations for discharge 158089, and modeled response using the resistive MHD code MARS-F for (c) $n = 3$ applied perturbations (d) $n = 2$ applied perturbations.

Figure 5 (color online): The average poloidal wavelength (m) of the kink eigenmode along the HFS of DIII-D, modeled using the resistive MHD code MARS-F, for both even parity $n = 2$ (solid blue diamonds) and $n = 3$ (open black diamonds) externally applied perturbations.

Figure 6 (color online): An $n = 2$ RMP ELM suppressed magnetic response bifurcation along the HFS of DIII-D showing (a) the combined $n = 1$ and $n = 2$ plasma response (Gauss), (b) the estimated widths of 8/2, 9/2, 10/2, 4/1 and 5/1 magnetic island chains (cm), (c) the phase (degrees) of the $n = 2$ and $n = 1$ modes, in which the $n = 1$ mode does not vary during ELM suppression while the $n = 2$ mode is entrained with the applied rotation of the applied field, and (d) the filterscope measured (D_α) divertor recycling light for discharge 158115.

Figure 7 (color online): (a) Contour of T_e (keV) vs major radius (m) and time (ms) showing a T_e decrease near the 4/1, 9/2 and 5/1 rational surfaces during a period of $n = 2$ RMP ELM suppression in discharge 158115. (b) The gradient of T_e (keV/m) showing a flat spot near the 9/2 and 5/1 rational surfaces that is not present prior to ELM suppression.

Figure 8 (color online): The total plasma pressure radial profiles for axisymmetric equilibria reconstructions before (solid) and after (dashed) $n = 2$ RMP ELM suppression. The major radius (m) of the $q = 4$ rational surface along the HFS and LFS is also shown. Discharge 158115.

FIGURES

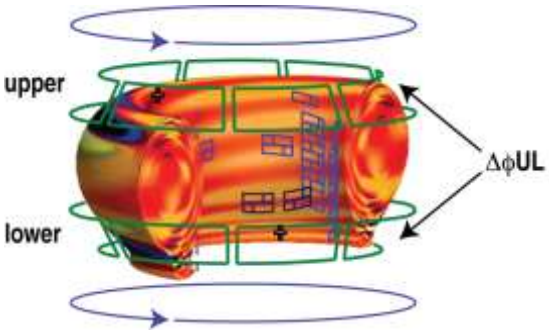

J.D. King Figure 1

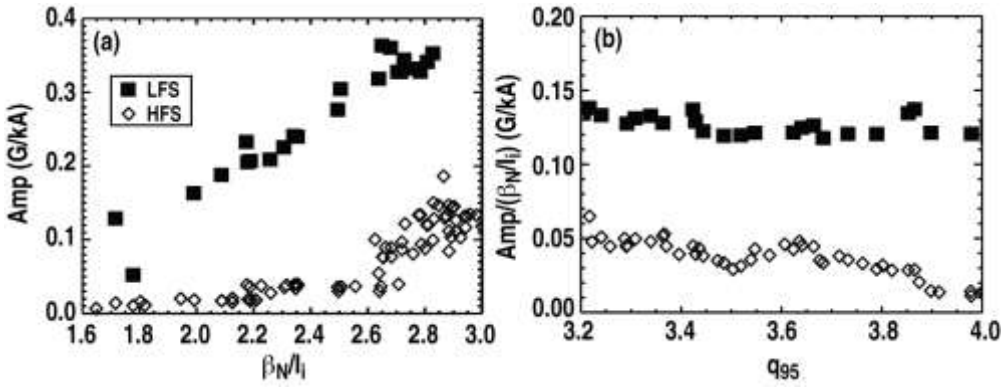

J.D. King Figure 2

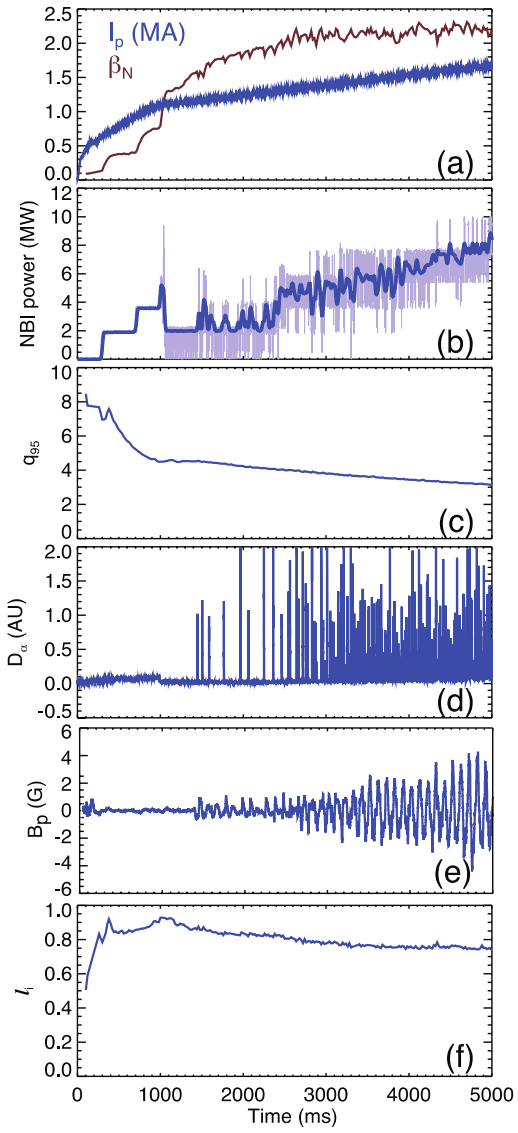

J.D. King Figure 3

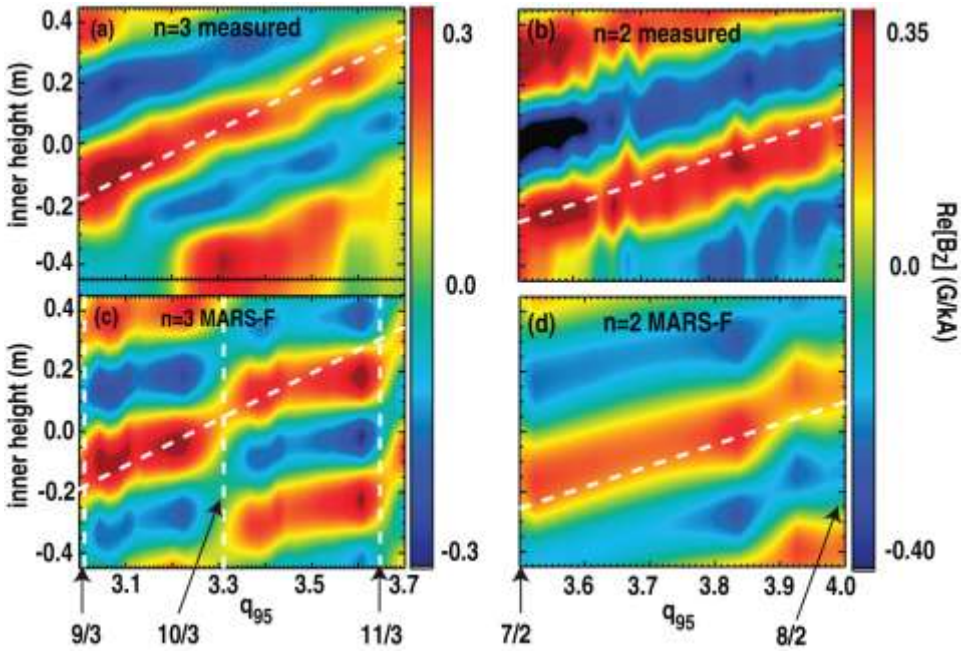

J.D. King Figure 4

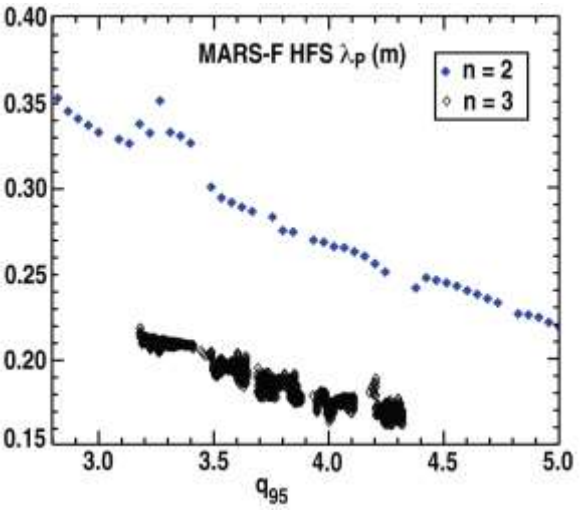

J.D. King Figure 5

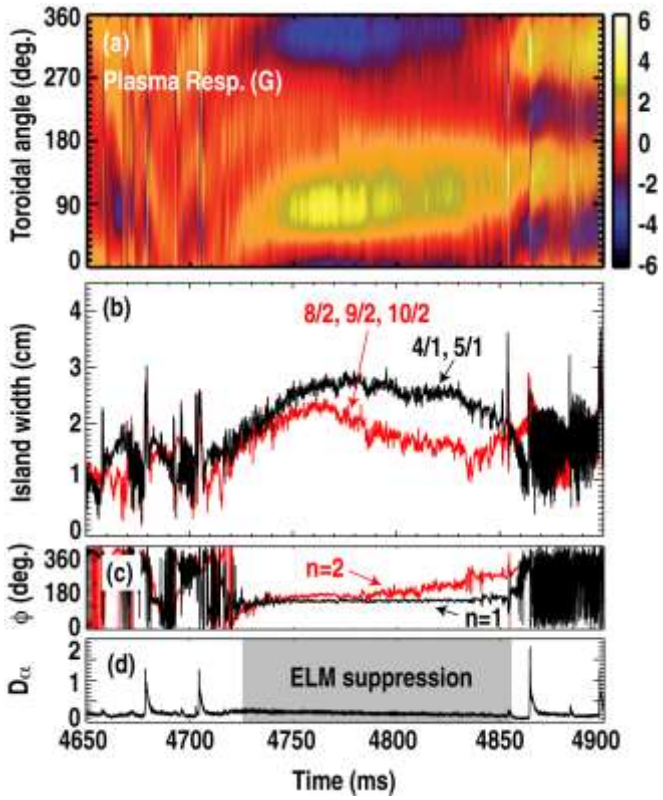

J.D. King Figure 6

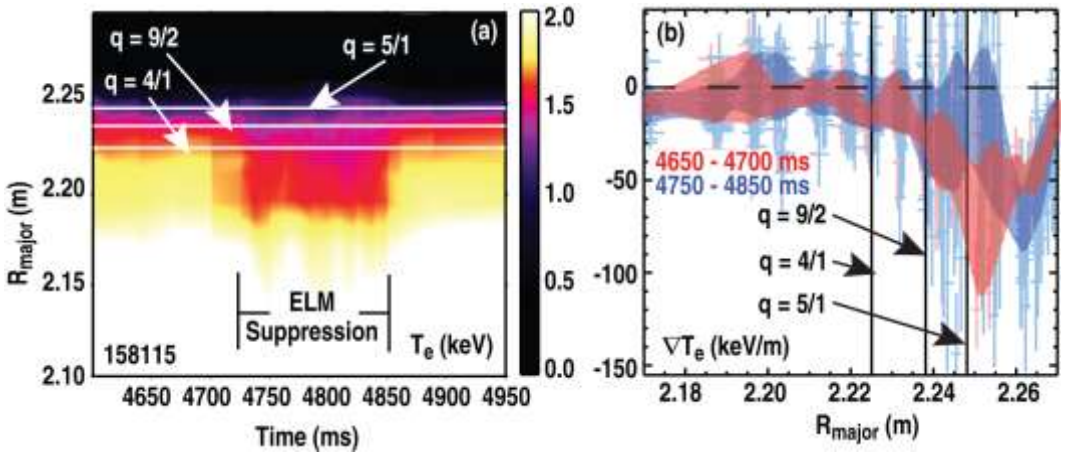

J.D. King Figure 7

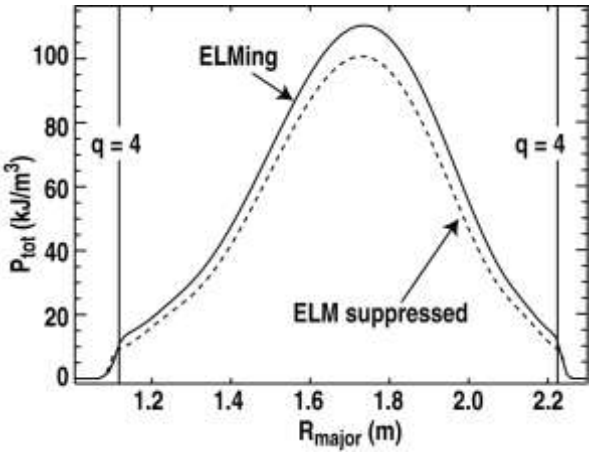

J.D. King Figure 8

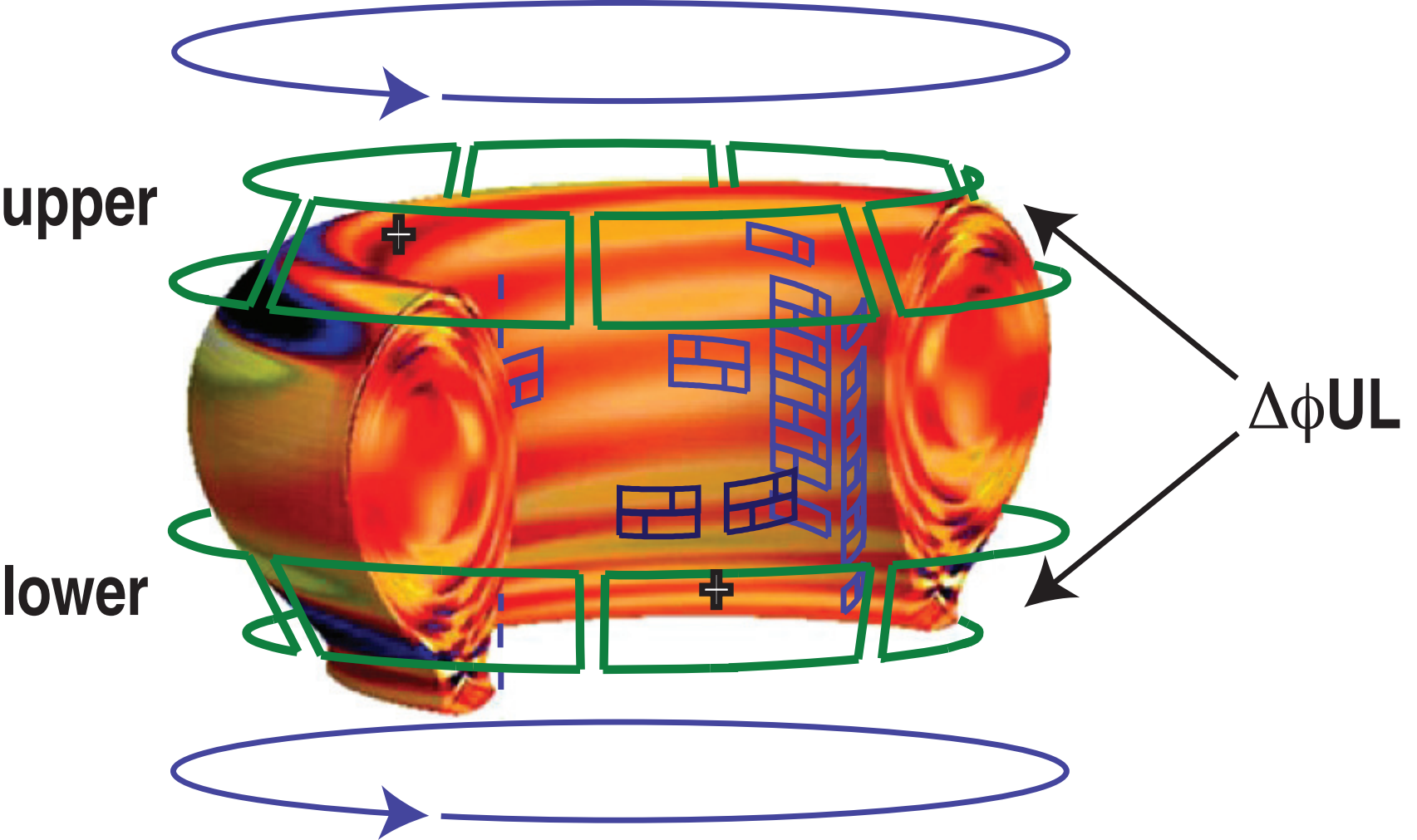
upper
lower
ΔϕUL

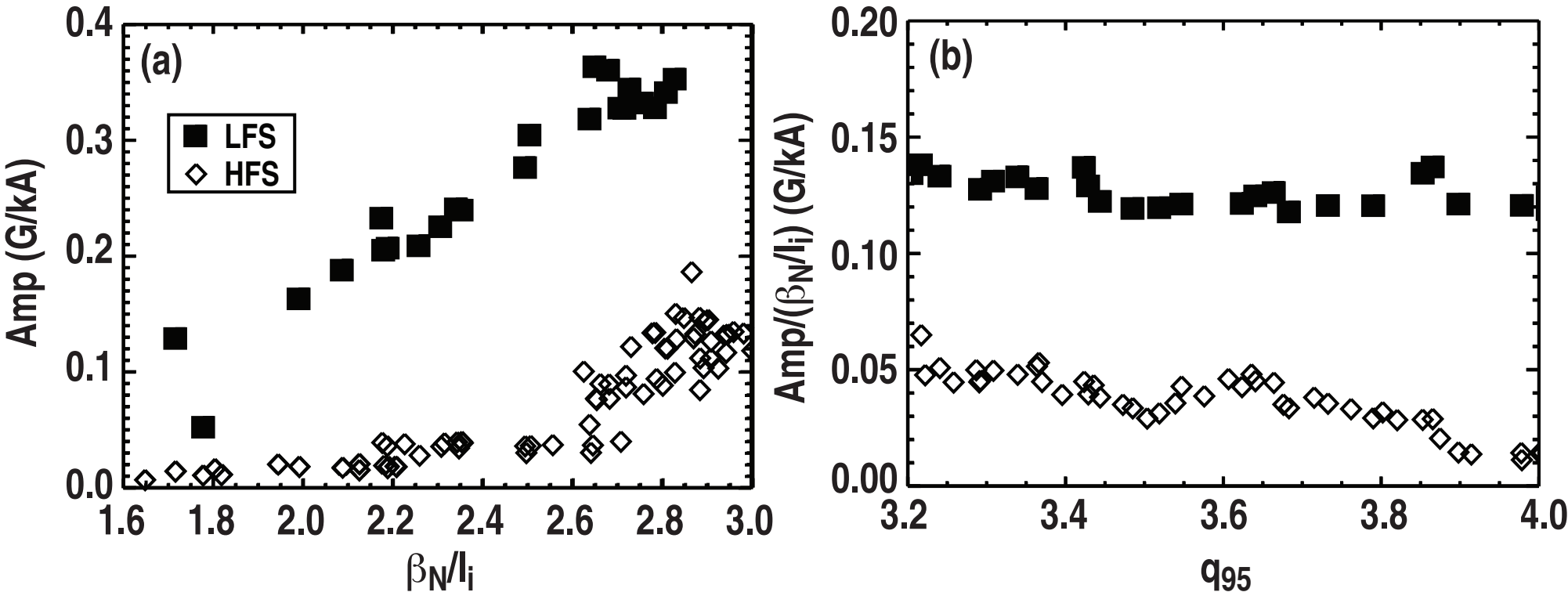
(a)
LFS
HFS
Amp (G/kA)
0.0
0.1
0.2
0.3
0.4
1.6
1.8
2.0
2.2
2.4
2.6
2.8
3.0
βN/li
(b)
Amp/(βN/li) (G/kA)
0.00
0.05
0.10
0.15
0.20
3.2
3.4
3.6
3.8
4.0
q95

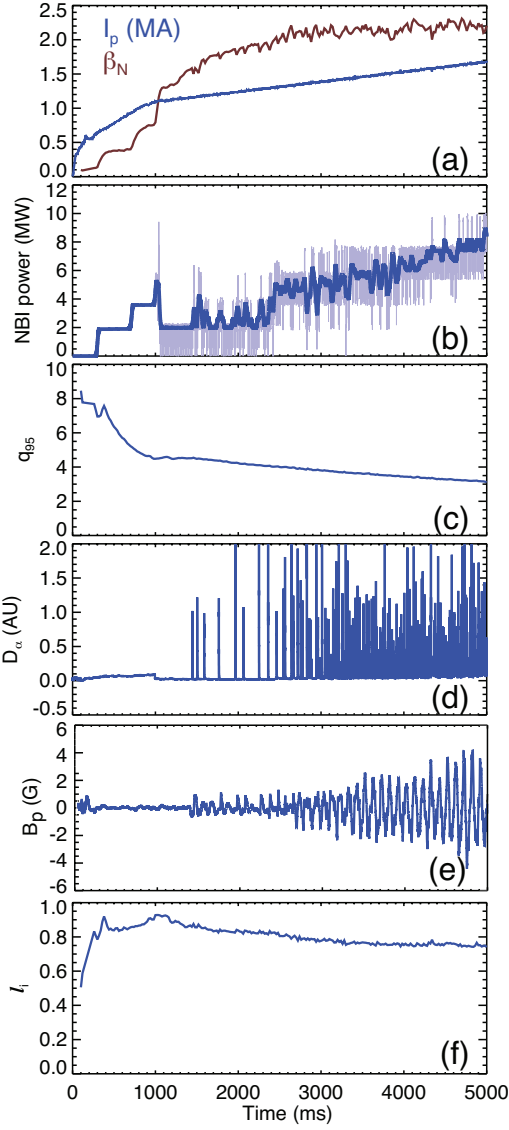
I_p (MA)
β_N
(a)
NBI power (MW)
(b)
q_{95}
(c)
D_α (AU)
(d)
B_p (G)
(e)
l_i
(f)
Time (ms)

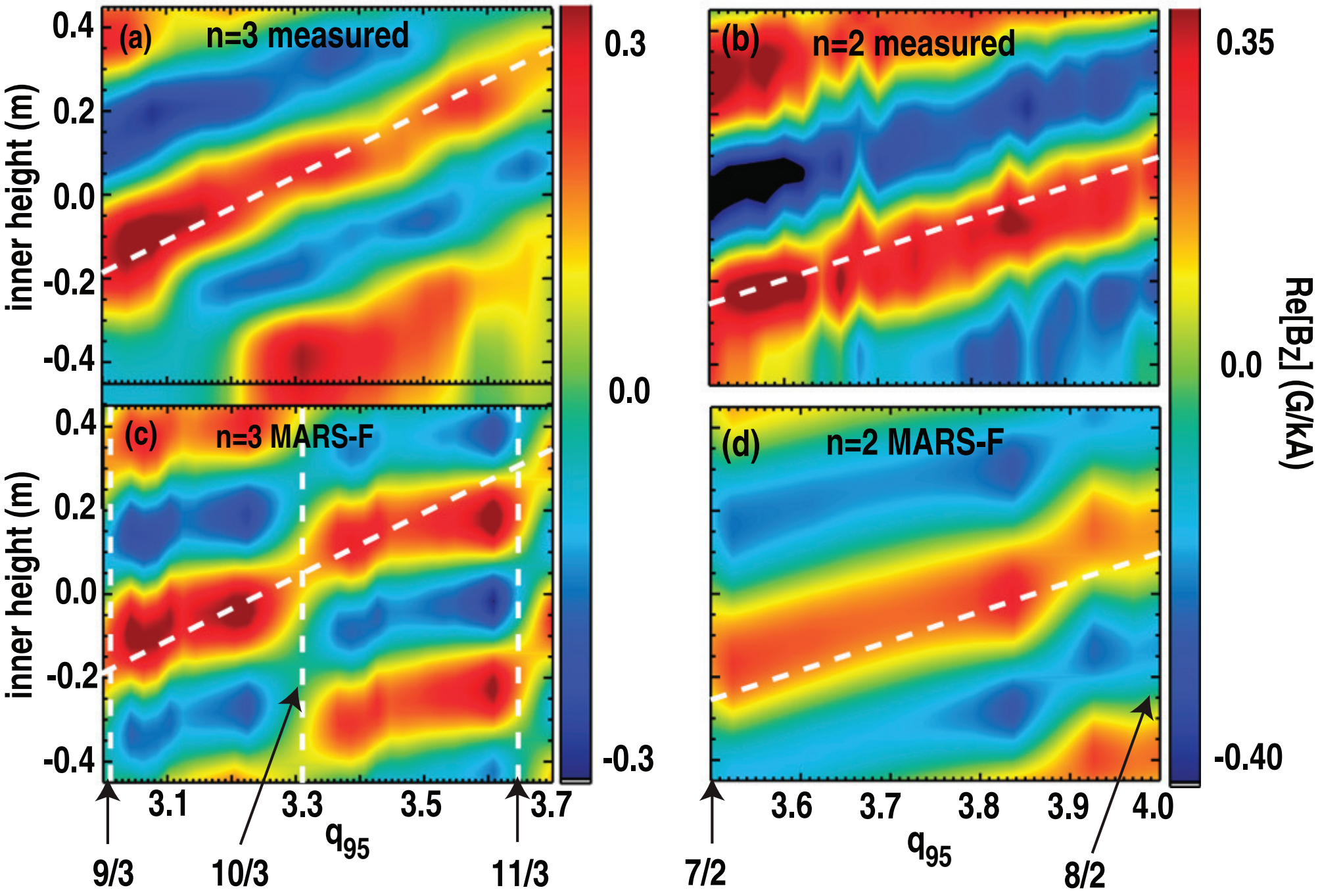
(a) n=3 measured
(b) n=2 measured
(c) n=3 MARS-F
(d) n=2 MARS-F
inner height (m)
0.4
0.2
0.0
-0.2
-0.4
0.3
0.0
-0.3
0.35
-0.40
Re[Bz] (G/kA)
3.1
3.3
3.5
3.7
3.6
3.7
3.8
3.9
4.0
q95
9/3
10/3
11/3
7/2
8/2

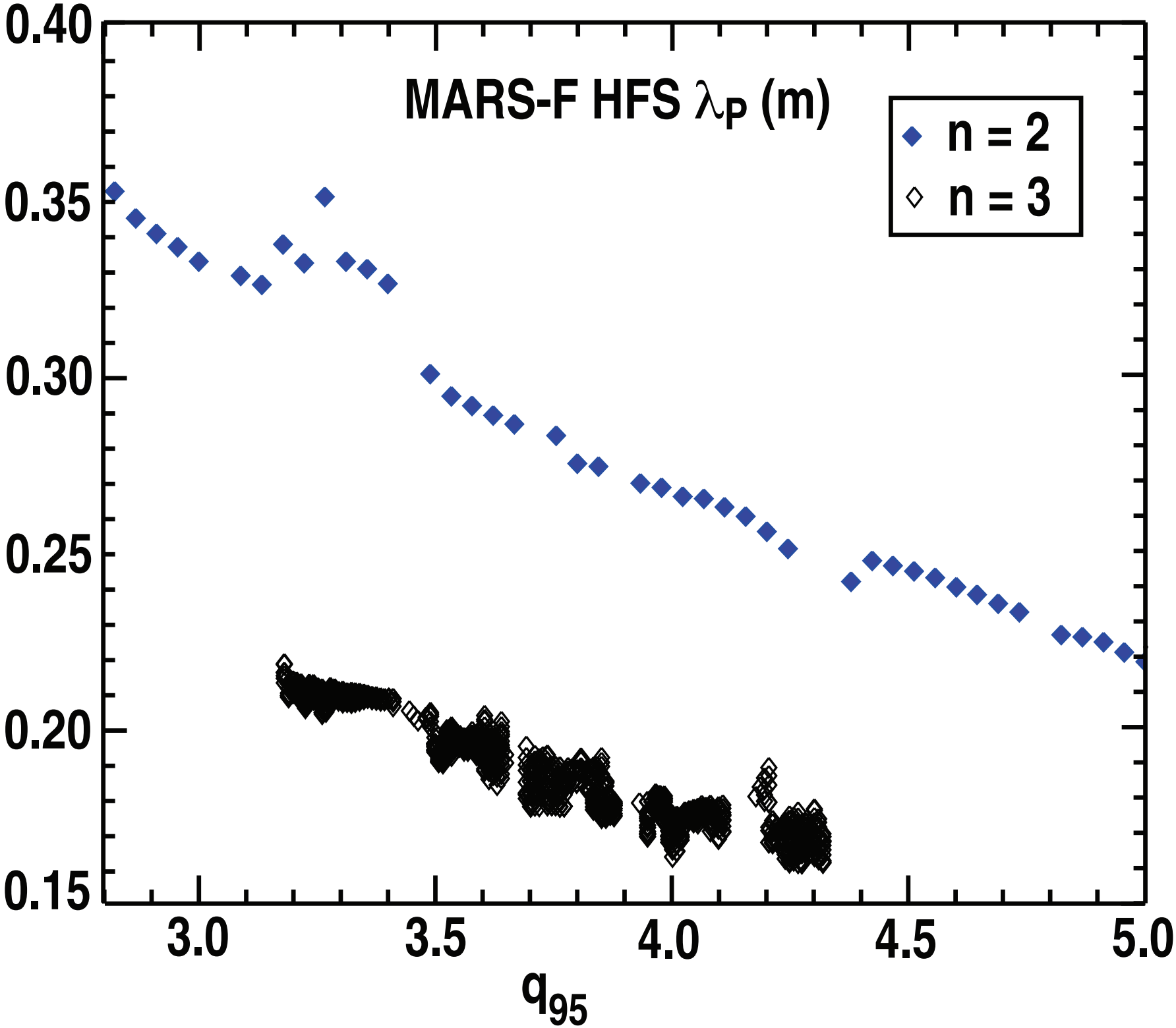
MARS-F HFS λP (m)
n = 2
n = 3
0.40
0.35
0.30
0.25
0.20
0.15
3.0
3.5
4.0
4.5
5.0
q95

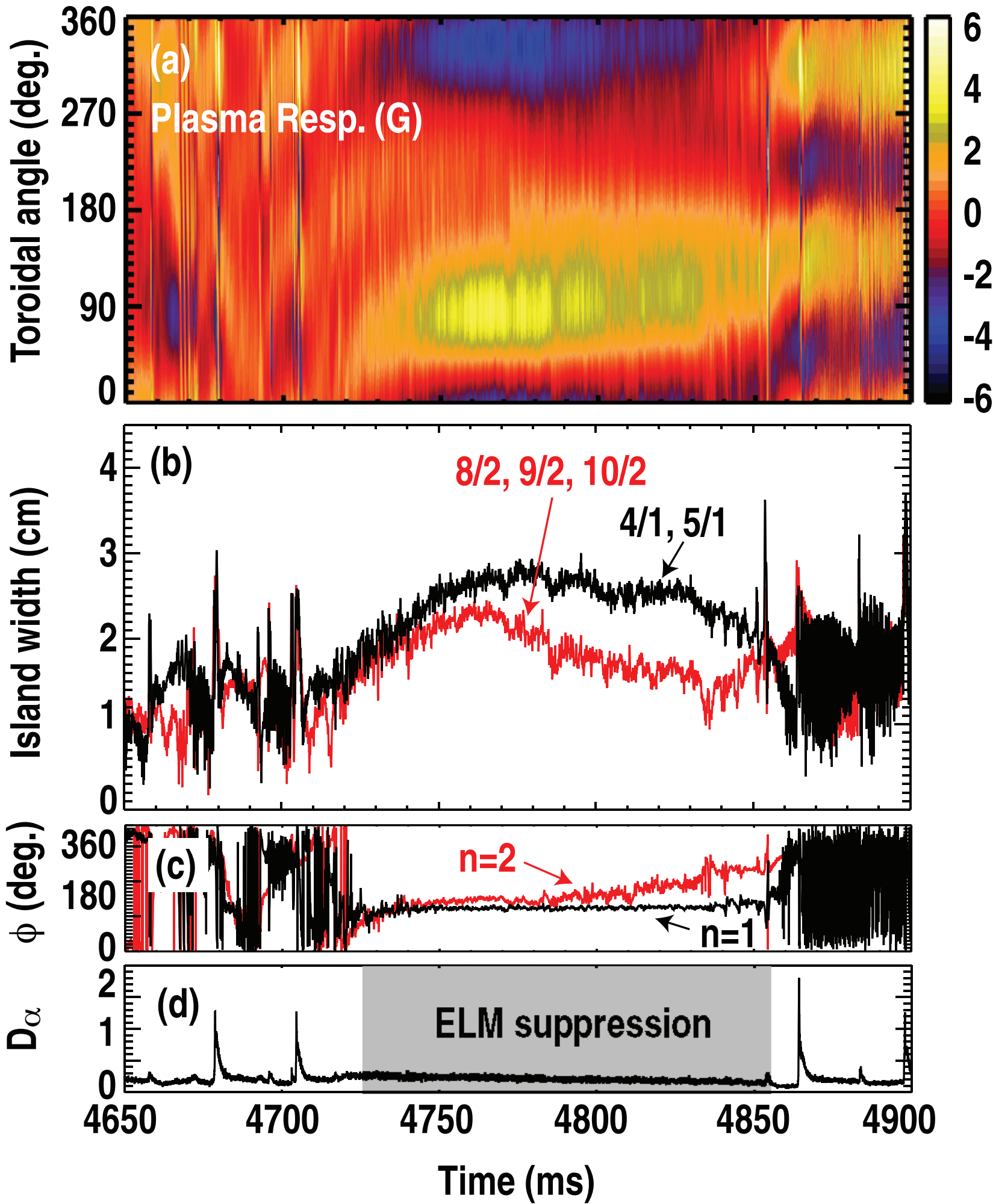
(a)
Plasma Resp. (G)
Toroidal angle (deg.)
360
270
180
90
0
6
4
2
0
-2
-4
-6
(b)
8/2, 9/2, 10/2
4/1, 5/1
Island width (cm)
4
3
2
1
0
(c)
n=2
n=1
ϕ (deg.)
360
180
0
(d)
ELM suppression
Dα
2
1
0
4650
4700
4750
4800
4850
4900
Time (ms)

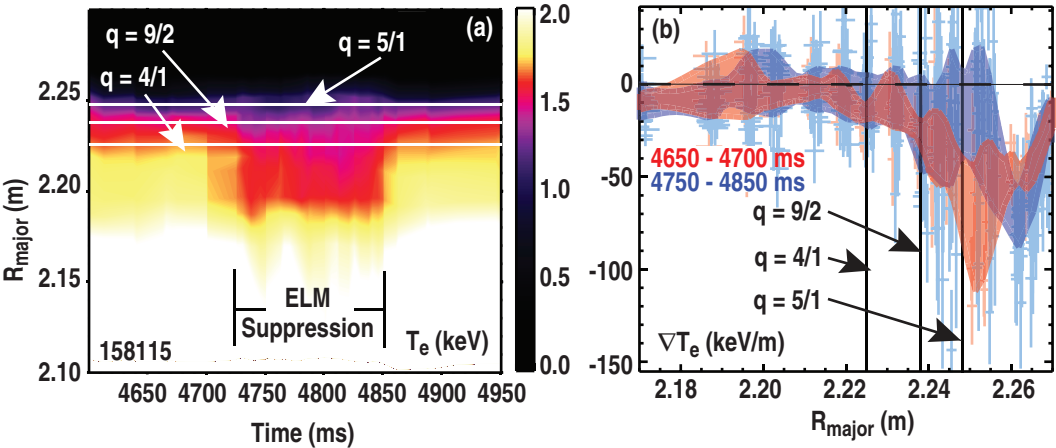
q = 9/2
q = 4/1
q = 5/1
(a)
2.25
2.20
2.15
2.10
R_major (m)
2.0
1.5
1.0
0.5
0.0
ELM
Suppression
158115
T_e (keV)
4650 4700 4750 4800 4850 4900 4950
Time (ms)
(b)
0
-50
-100
-150
4650 - 4700 ms
4750 - 4850 ms
q = 9/2
q = 4/1
q = 5/1
∇T_e (keV/m)
2.18 2.20 2.22 2.24 2.26
R_major (m)

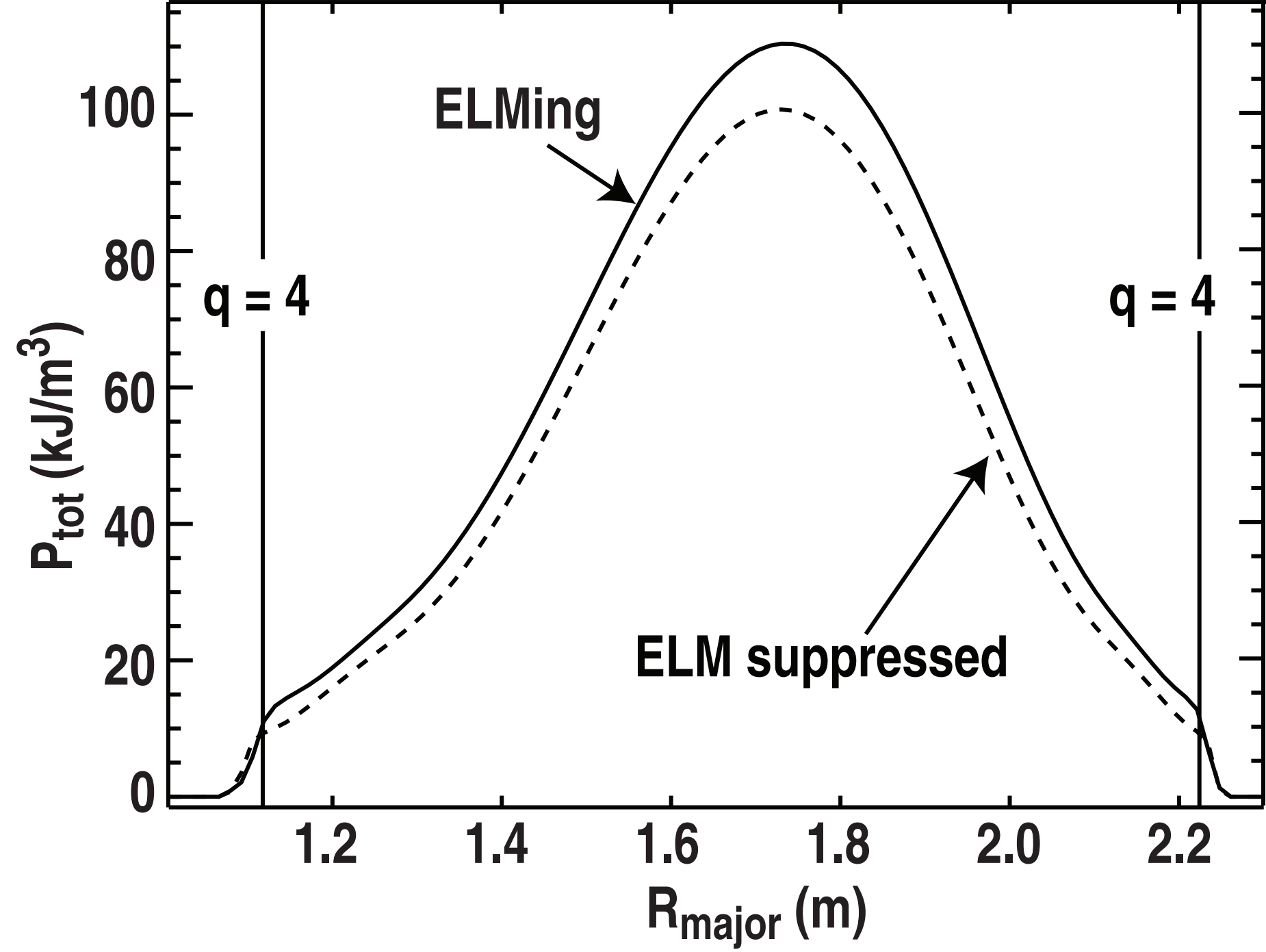
ELMing
ELM suppressed
q = 4
q = 4
100
80
60
40
20
0
1.2
1.4
1.6
1.8
2.0
2.2
P_{tot} (kJ/m^3)
R_{major} (m)